Dalton Transactions

PAPER

View Article Online
View Journal | View Issue

Open Access Article. Published on 30 2022. Downloaded on 29.09.2024 10:23:06.
This article is licensed under a Creative Commons Attribution 3.0 Unported Licence.

Cite this: *Dalton Trans.*, 2022, **51**, 15974

Texture evolution in rhombohedral boron carbide films grown on 4H-SiC(000$\bar{1}$) and 4H-SiC(0001) substrates by chemical vapor deposition†

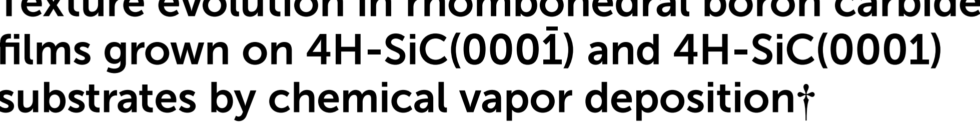

Laurent Souqui, ‡ Sachin Sharma, Hans Högberg and Henrik Pedersen *

Received 1st July 2022,
Accepted 29th September 2022

DOI: 10.1039/d2dt02107b

rsc.li/dalton

Boron carbide in its rhombohedral form (r-B_xC), commonly denoted B_4C or $B_{13}C_2$, is a well-known hard material, but it is also a potential semiconductor material. We deposited r-B_xC by chemical vapor deposition between 1100 °C and 1500 °C from triethylboron in H_2 on 4H-SiC(0001) and 4H-SiC(000$\bar{1}$). We show, using ToF-ERDA, that pure B_4C was grown at 1300 °C, furthermore, using XRD that graphite forms above 1400 °C. The films deposited above 1300 °C on 4H-SiC(000$\bar{1}$) were found to be epitaxial, with the epitaxial relationships $B_4C(0001)[10\bar{1}0]\|$4H-SiC$(000\bar{1})[10\bar{1}0]$ obtained from pole figure measurements. In contrast, the films deposited on 4H-SiC(0001) were polycrystalline. We suggest that the difference in growth mode is explained by the difference in the ability of the different surfaces of 4H-SiC to act as carbon sources in the initial stages of the film growth.

Introduction

Due to its high hardness of about 35 GPa,[1] rhombohedral boron carbide, commonly denoted B_4C or $B_{13}C_2$, here referred to as r-B_xC ($4 \leq x \leq 10.5$), is mainly used as a super hard material in applications such as abrasive or plate armour.[2] Additionally, owing to the self-healing capabilities of the boron icosahedra under energetic bombardment[3] and due to the high neutron cross-section of the isotope ^{10}B, it is a promising material for boron-based neutron detectors.[4] Interestingly, and less explored, is that r-B_xC is a semiconductor with electronic properties which can be tuned with the B : C stoichiometry.[5–7] Its bandgap, for instance, ranges from 0.48 to 2.1 eV with increasing boron content.[5–7] Semiconducting r-B_xC could be used in combination with the wide bandgap materials boron subphosphide ($B_{12}P_2$)[8] and boron subarsenide ($B_{12}As_2$),[9] with which it shares structural similarities, and would enable the fabrication of novel radiation resistant heterostructures. In addition, r-B_xC is interesting for thermoelectric devices due to its high temperature thermoelectric properties, with a high thermal conductivity (4–10 W m^{-1} K^{-1}) and high Seebeck coefficient (150 to 300 μV K^{-1} between 500–1000 °C).[4,10] Furthermore, another peculiarity of boron carbide is its ability to form crystals with five-fold symmetry due to crystal twinning.[11,12] Controlled formation of these twinned crystals could be used to approximate and study boron-carbide-based quasicrystals. However, to fully explore r-B_xC as a semiconductor, thin films with high crystalline quality, preferably epitaxially grown are needed, but the growth of epitaxial r-B_xC crystals has proved to be challenging[13] using vapor phase deposition techniques.

Using chemical vapor deposition (CVD) with the single-source precursor triethylboron (TEB) in an H_2 ambient in the temperature range of 1100 to 1500 °C, we investigate the growth conditions for r-B_xC films on the Si-terminated (4H-SiC (0001)) and C-terminated (4H-SiC(000$\bar{1}$)) faces. We report epitaxial growth on the 4H-SiC(000$\bar{1}$) at 1300 °C, while deposition on 4H-SiC(0001) yields polycrystalline films at the same temperature.

Experimental details

Film deposition

Thin films of r-B_xC were deposited on 4H-SiC substrates in a hot-wall horizontal CVD reactor from pyrolysis of 0.7 SCCM triethylboron (TEB, $B(CH_2CH_3)_3$, 99.99%, SAFC HiTech) in 5700 SCCM hydrogen gas (H_2, Palladium membrane purified) for 180 min. The process pressure was regulated to 7000 Pa by a throttle valve and the deposition temperature of 1100–1500 °C, monitored by a pyrometer (Heitronics KT81R, calibrated by silicon melting). The influence of the residence time was studied by either changing the total flow or by utilizing the

Department of Physics, Chemistry and Biology, Linköping University, SE-581 83 Linköping, Sweden. E-mail: henrik.pedersen@liu.se

† Electronic supplementary information (ESI) available. See DOI: **https://doi.org/10.1039/d2dt02107b**

‡ Present address: Department of Materials Science and Engineering, University of Illinois at Urbana-Champaign, 1304 W. Green St. MC 246, Urbana, Illinois 61801, USA.

This journal is © The Royal Society of Chemistry 2022

Open Access Article. Published on 30 2022. Downloaded on 29.09.2024 10:23:06. This article is licensed under a Creative Commons Attribution 3.0 Unported Licence.

position of the substrates in the SiC-coated elliptical graphite susceptor.

The temperature distribution and the residence times in the susceptor were evaluated using COMSOL Multiphysics (version 5.2). The susceptor was modelled using a 2D axisymmetric approximation. Since TEB is highly diluted in H_2, a flow of pure H_2 was considered in these calculations. The temperature profile inside the susceptor (without flow) was described by a parabolic function, as previously calculated for this reactor by Danielsson.[14] The residence time t_{res} at a given point x_i was defined using the formula:

$$t_{res}(x_i) = \int_{x_{inlet}}^{x_i} \frac{dx}{v(x)}$$

where x is a variable coordinate along the length of the susceptor, x_{inlet} is the coordinate at the inlet of the susceptor and $v(x)$ is the calculated gas velocity at the distance.

Prior to deposition, the 4H-SiC wafers were sawn into 10 × 10 mm^2 pieces. The orientations of the 4H-SiC substrates used were 4H-SiC(0001) and 4H-SiC(000$\bar{1}$) which conventionally refers to the Si-terminated and C-terminated sides, respectively. The offcut relative to the c-axis was ±0.5° (commonly referred as on-axis). Prior to deposition, the substrates were degreased in acetone for five minutes followed by ethanol for five minutes, both using an ultrasonic bath. This cleaning step was followed by a standard cleaning procedure for semiconductors with etching in oxidating alkaline solution (ammonia solution (25%), hydrogen peroxide solution (48%) and water in respective proportions 1 : 1 : 5) at 80 °C for five minutes followed by a rinse in deionized water and further treatment in hot oxidizing acidic solution (hydrochloric acid solution (37%), hydrogen peroxide (48%) and water in respective proportions 1 : 1 : 6) at 80 °C for five minutes and finally a rinse in deionized water. Additionally, the substrates used for the lowest deposition (1100 °C) temperature were dipped in 2% HF solution to ensure the removal of the native silicon dioxide.

Film characterization

X-ray diffraction (XRD) was performed using Cu Kα radiation. The $2\theta/\omega$ diffractograms were recorded using an X'Pert Pro diffractometer equipped with a Bragg–Brentano HD optics with 1/2° divergence slit as primary optics and a X'celerator detector with 5 mm anti-scatter slit, 0.4° Soller slits and Kβ Ni filter as secondary optics. XRD ω-scan (rocking curve measurements) are obtained using the PANAlytical Empyrean MRD and the measurements were performed by using capillary optics (X-ray lens) with a 2 × 2 mm mask on primary optics and a parallel plate collimator with 0.27° slit and a Ni filter as secondary optics. Since the X-Ray lens is not a monochromatic optic module, the use of a Ni filter was necessary to suppress the Cu Kβ line. The integral breadth was obtained by fitting the rocking curves with Pearson VII functions using the fityk software (version 1.3.1). XRD φ-scans and pole figures were recorded using an X'Pert MPD diffractometer equipped with 2 × 2 mm^2 cross-slits and a Kβ Ni filter as primary optics and a proportional detector (PW1711/96) with a parallel plate collimator and a 0.27° slit as secondary optics.

Fourier transform infrared spectroscopy (FTIR) reflectance spectra were measured in a Bruker VERTEX 70 equipment with incident s-polarized light at an angle of 60° with respect to the sample surface normal. The spectra were acquired in reflectance configuration at incidence angle of 30° with respect to the surface normal, a resolution of 2 cm^{-1} and s-polarization. The measurements were conducted at room temperature, after a 30 min N_2 purge, with 2 cm^{-1} resolution and averaged over 50 scans. A thin film of gold was used as reference.

Scanning electron microscopy (SEM) was used to study the surface morphology of the films. The microscope used was a Zeiss Gemini. All the micrographs were acquired using an accelerating voltage of 5 kV and an in-lens detector. SEM was also used for thickness measurements of the B_xC films deposited on the 4H-SiC(0001); these measurements were performed on the aligned cross sections of the samples. The samples were scratched using a diamond tipped pen and then cracked. The thickness of B_xC film grown at 1100 °C was determined to be around 900 nm, those grown at 1200 °C, 1300 °C was around 1.5 μm, the film grown at 1400 °C was about 1.6 μm and the film grown at 1500 °C was determined around 3 μm.

The compositional analysis of selected films was performed using time-of-flight energy elastic recoil detection analysis (ToF-ERDA). The measurements were done using a 36 MeV $^{127}I^{+8}$ beam. The incidence angle of primary ions and exit angle of recoils were both 67.5° to the sample surface normal constituting a recoil angle of 45°. The time-of-flight vs energy loss map is also utilized, this has better separation for lighter elements (B and C). The measured ToF-ERDA spectra data was then converted into relative atomic concentration profiles using the Potku code.[15]

Results

Boron carbide deposition on C-face 4H-SiC(000$\bar{1}$)

From the XRD diffractograms in Fig. 1, it is evident that films deposited at 1100 and 1200 °C are polycrystalline, as seen from the additional reflections from crystal planes other than (0003) and higher order diffractions. For higher temperatures, the films are oriented along [0003] since no reflections from crystal planes other than (0003) and higher order diffractions are visible in the diffractograms. As the information provided by the $2\theta/\omega$ scans is confined to planes that are parallel to the sample surface, XRD pole figure measurement was performed to assess the degree of in-plane orientation with respect to the substrate. The distinct poles in the pole figure measurement in Fig. 2, shows that the r-B_xC films are not only c-axis oriented, but grown epitaxially on the 4H-SiC(000$\bar{1}$). The epitaxial relationships were determined as r-B_xC(0001)[10$\bar{1}$0]|| 4H-SiC(000$\bar{1}$)[10$\bar{1}$0]. The six poles, separated by 60°, show that the films are twinned. This is expected due to the higher sym-

Open Access Article. Published on 30 2022. Downloaded on 29.09.2024 10:23:06.
This article is licensed under a Creative Commons Attribution 3.0 Unported Licence.

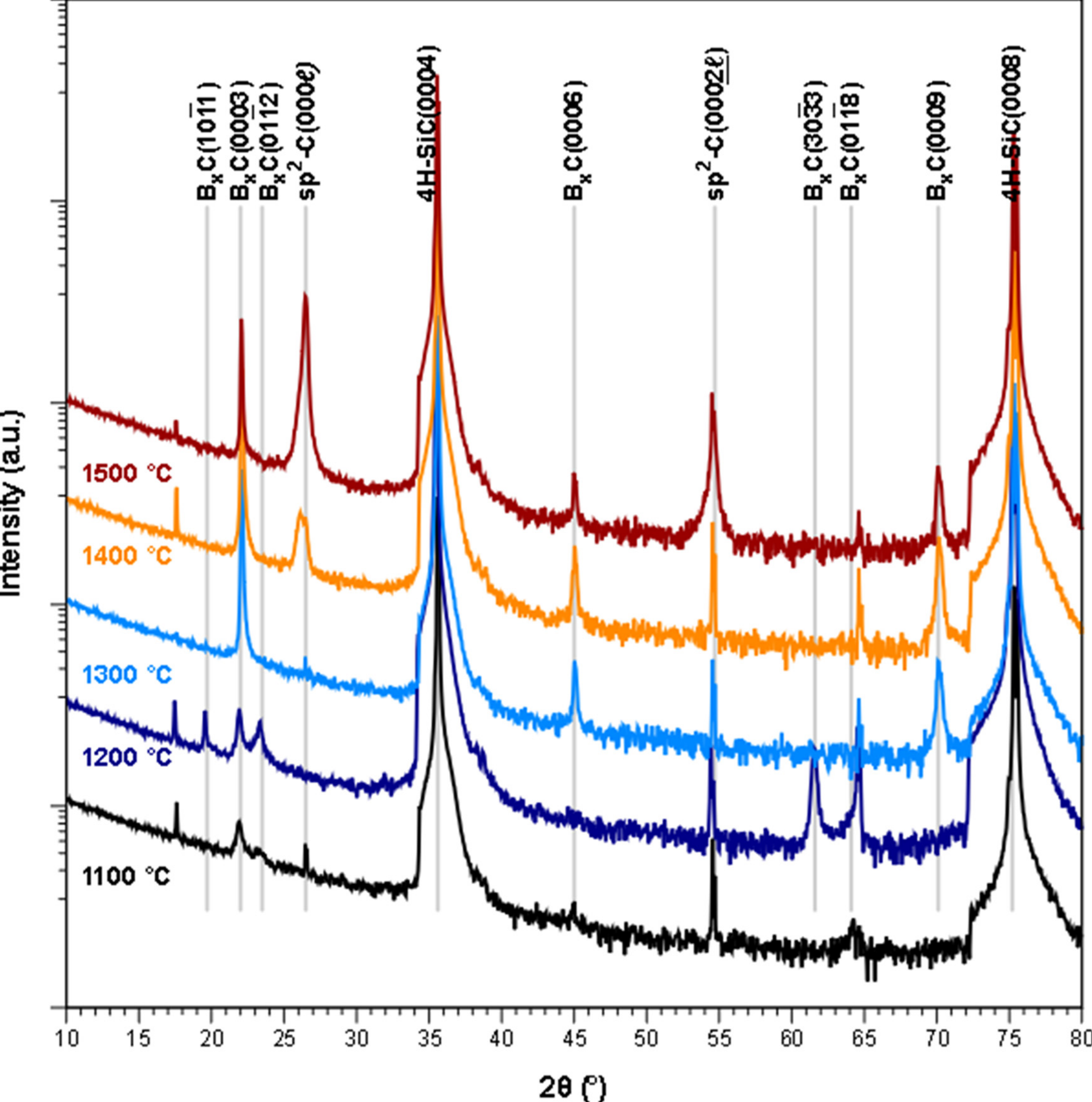

Fig. 1 XRD 2θ/ω diffractograms of r-B_xC films deposited on 4H-SiC(000$\bar{1}$) at temperatures (from bottom to top) of 1100, 1200, 1300, 1400 and 1500 °C. The low intensity, non-indexed sharp peaks are the forbidden 4H-SiC(000ℓ) diffraction peaks.

metry of the hexagonal 4H-SiC substrate compared to the r-B_xC crystal of rhombohedral symmetry.

FTIR further supports the XRD data; as observed, the chain stretching mode disappears for r-B_xC grown on the C-face compared to r-B_xC grown on the *Si*-face in Fig. S1,‡ which is consistent with the triatomic chains being perpendicular to the electric field (s-polarized light). The onset of graphite formation is observed from the appearance of sp^2-C(000ℓ) peaks at 1400 °C in Fig. 1. r-B_xC and pyrolytic graphite where found to grow to a similar extent and in a similar fashion, as seen from a comparison of the intensity of r-B_xC(0003) and sp^2-C(000ℓ)) in Fig. 1, and from the top-view micrograph in Fig. 4. Rocking curve measurements of the (0003) planes for samples deposited above 1300 °C (Fig. 3) show a sharp component whose integral breadth is comparable to the substrate as well as a much broader component which decreases as the deposition temperature increases. Rocking curve measurements allows evaluation of the overall degree of alignments of the crystallites along the [001] and [101] directions. The dispersion [001] direction is associated to the tilting of the grains with respect to the vicinal surface normal while [101] comprises an additional rotational component referred as twisting. Further information about the differences in crystal quality between the films grown at the examined temperatures, as determined using rocking curves, is expressed in Fig. 3d.

Plan view SEM (Fig. 4) show that the films deposited on C-face 4H-SiC at 1100 °C (Fig. 4a) and 1200 °C (Fig. 4b) were highly facetted and polycrystalline while the films deposited at higher temperatures were smoother. The films deposited at 1300 °C (Fig. 4c) and 1400 °C (Fig. 4) constituted of percolated

 This journal is © The Royal Society of Chemistry 2022

Open Access Article. Published on 30 2022. Downloaded on 29.09.2024 10:23:06.
This article is licensed under a Creative Commons Attribution 3.0 Unported Licence.

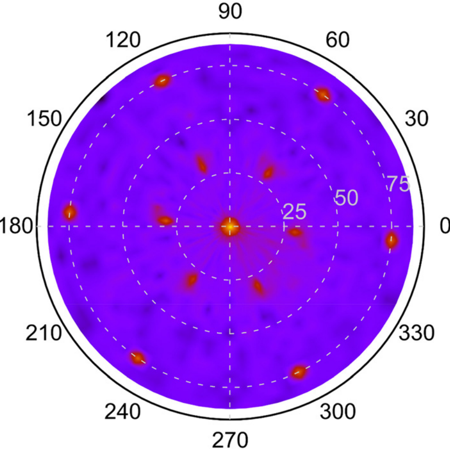

Fig. 2 X-ray pole figure of the r-$B_xC\{10\bar{1}4\}$ plane family (2θ = 35.08°, ψ = 31.81°) of a r-B_xC film deposited at 1300 °C on 4H-SiC(000$\bar{1}$), showing the epitaxial relationship with the substrate (4H-SiC{10$\bar{1}\bar{1}$} at 2θ = 34.84°, ψ = 75.17°) and rotational twinning. The strong pole at the center originates from the tail of 4H-SiC{000$\bar{1}$} (2θ = 35.6°, ψ = 0°).

islands and continuous films were obtained at 1500 °C (Fig. 4e). The continuous films comprised distinct areas of boron carbide and graphite and hexagonal defects were observed for both materials (Fig. 5).

The sample deposited at 1300 °C was selected for compositional analysis as it was not contaminated with graphite (as seen from Fig. 1). ToF-ERDA yielded B to C ratio of 4 : 1 (B – 79.2 at% ± 0.8 at%, C – 20.5 at% ± 0.4 at%) and with around 0.3 at% of O and H below the detection limit of the technique.

Boron carbide deposition on *Si*-face 4H-SiC(0001)

Deposition on *Si*-face 4H-SiC(0001) substrates resulted in polycrystalline rhombohedral boron carbide as seen from the $2\theta/\omega$ diffractogram (Fig. 6) and FT-IR reflectance spectra (Fig. S2‡) of a film deposited at 1400 °C. Pyrolytic graphite could also be detected under some conditions (Fig. 7). The orientation of the r-B_xC crystals and formation of graphite were found to be strongly dependent on the growth temperature and on the residence time of the gas in the susceptor, as presented in Fig. 7. The residence time at a given temperature was varied by placing the sample at different positions in the susceptor.

Regardless the deposition temperature, the B_xC films deposited at low residence times (below 0.10 s) were polycrystalline with no preferred orientation in contrast with the films deposited at longer residence times which showed preferred orientation. For residence times between 0.10 and 0.12 s this orientation evolved from [02$\bar{2}$1] at 1200 °C, to [0003] at 1300 °C to [10$\bar{1}$4] at 1400 °C, with a minor contribution of the (20$\bar{2}$5) planes in all cases, as shown in Fig. 7. For longer residence times (0.14 s), only the [0003] direction is favored at all temperatures. Finally, we found that the onset of pyrolytic graphite formation occurs at around 1400 °C and for residence times around 0.09 s and becomes the dominant phase at higher temperatures and residence times.

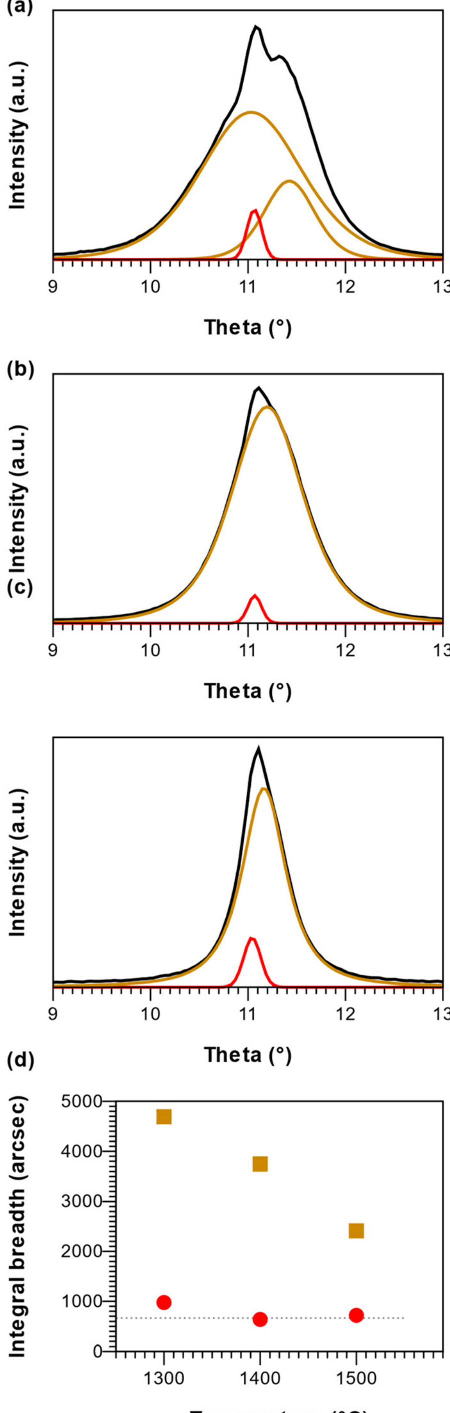

Fig. 3 X-ray rocking curve (in black) of the r-B_xC(0003) planes r-B_xC film deposited at (a) 1300 °C, (b) 1400 °C and (c) 1500 °C on 4H-SiC (000$\bar{1}$). The sharp and broad components are shown in red and orange, respectively. (d) Integral breadth of the broad (orange squares) and sharp (red circles) components; the integral breadth of the asymmetric broad component at 1300 °C was calculated from the convolution of the two components shown in (a). The dotted grey line represents the averaged integral breadth for the rocking curves of 4H-SiC(0004) planes measured on each sample.

Open Access Article. Published on 30 2022. Downloaded on 29.09.2024 10:23:06.
This article is licensed under a Creative Commons Attribution 3.0 Unported Licence.

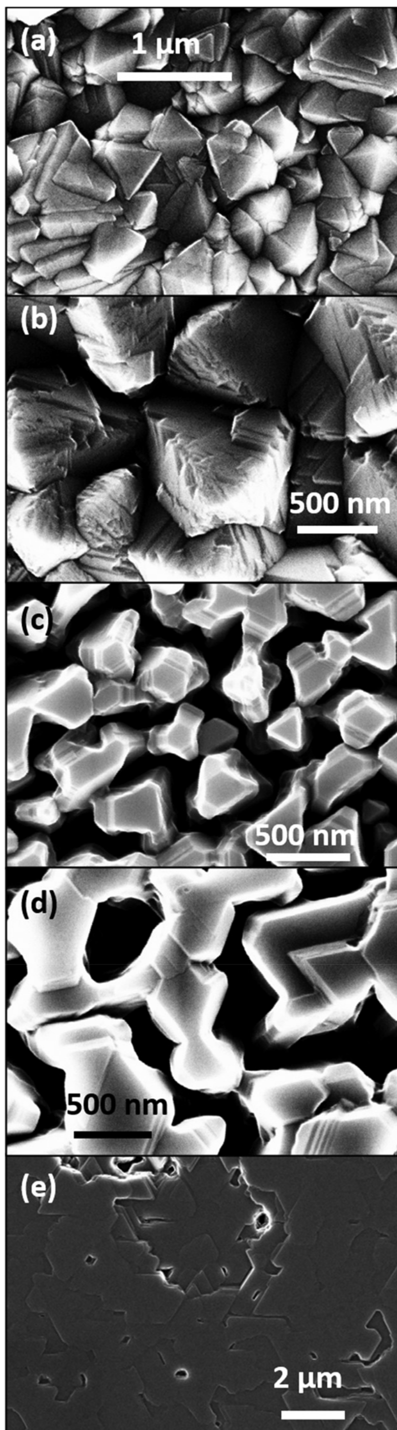

Fig. 4 Plan view SEM of rhombohedral boron carbide deposited on 4H-SiC(000$\bar{1}$); at (a) 1100 °C, (b) 1200 °C, (c) 1300 °C, (d) 1400 °C and (e) 1500 °C.

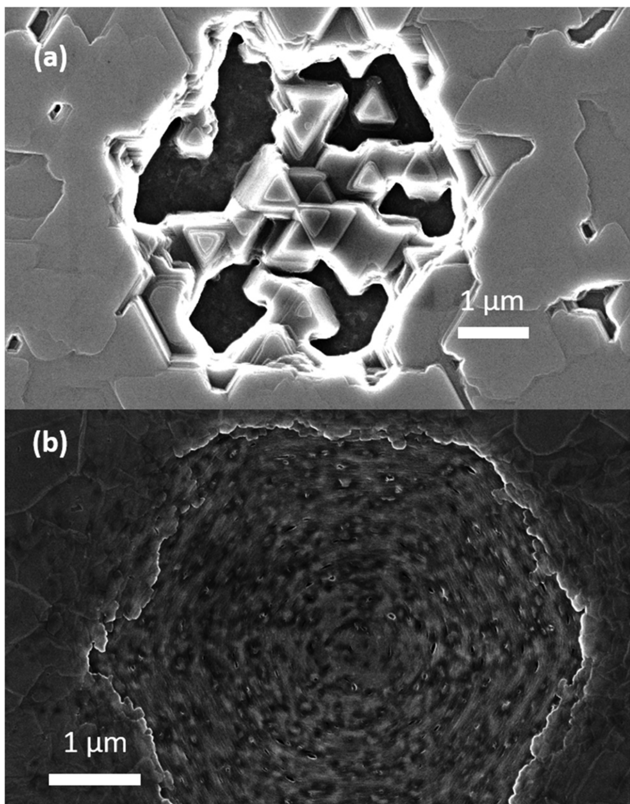

Fig. 5 Plan view SEM of the defects observed (a) rhombohedral boron carbide film and (b) pyrolytic graphite co-deposited at 1500 °C on 4H-SiC(000$\bar{1}$).

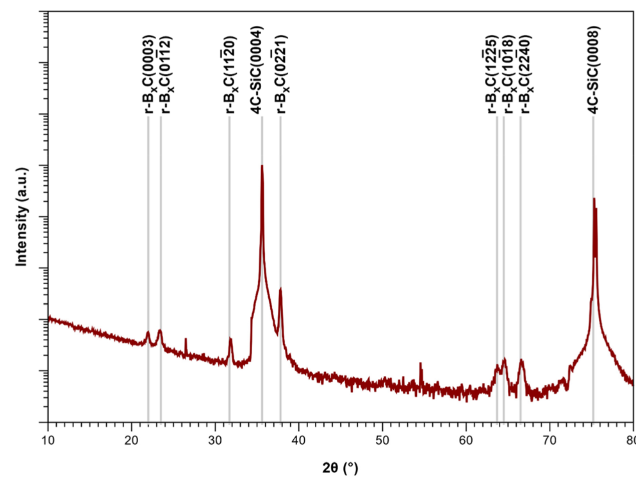

Fig. 6 2θ/ω diffractogram of a polycrystalline B$_x$C deposited at 1400 °C close to the inlet of the susceptor, corresponding to a residence time of 0.06 s. The sharp low-intensity non-indexed peaks come from the substrate.

A pole figure of the {10$\bar{1}$4} planes (2θ = 35.08°) of a r-B$_x$C film deposited at 1400 °C and 0.1 s residence time is shown in Fig. 8. This film is polycrystalline, mainly orientated along the [10$\bar{1}$4] direction, and graphite-contaminated, as seen in Fig. 7. The pole figure shows three concentric patterns. The outer most pattern, consists in 6 poles at $\psi \approx 75°$, which as for Fig. 2, originates from the substrate and are the tails of 4H-SiC {10$\bar{1}$1}. The second pattern at $\psi \approx 60°$ appears to be five-fold. This may seem counterintuitive considering two aspects: (1)

Open Access Article. Published on 30 2022. Downloaded on 29.09.2024 10:23:06.
This article is licensed under a Creative Commons Attribution 3.0 Unported Licence.

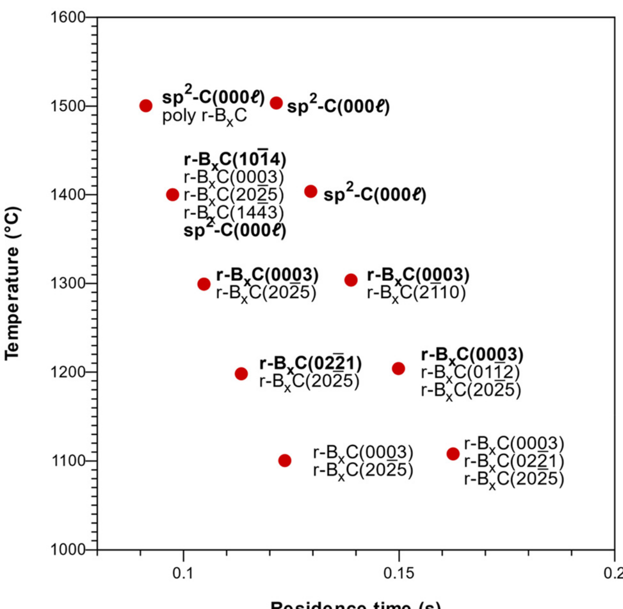

Fig. 7 Evolution of the orientation, from $2\theta/\omega$ XRD, of the r-B_xC films deposited on 4H-SiC(0001) substrates placed at the center and the backside of the susceptor. Bold face marks the dominating orientations. The corresponding residence times and temperatures were estimated by modeling.

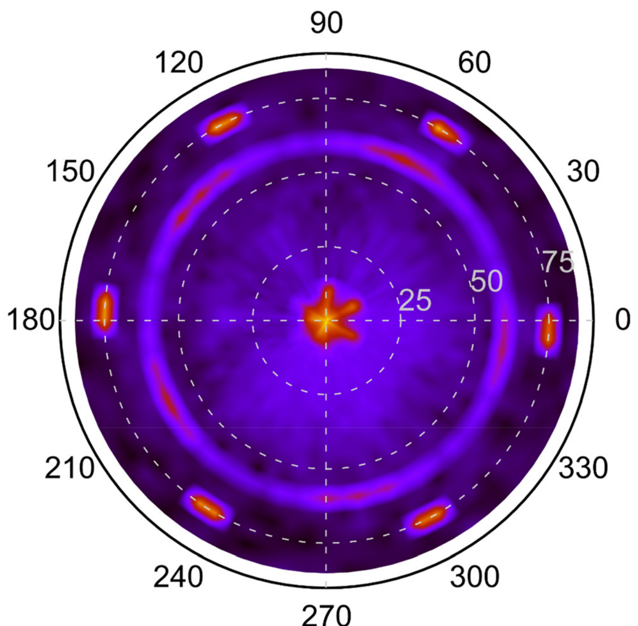

Fig. 8 Pole figure of the r-B_xC\{10$\bar{1}$4\} plane family (2θ = 35.08°, ψ = 60°) of a r-B_xC film deposited at 1400 °C on 4H-SiC(0001), showing a five-fold pattern and its orientation with respect to the substrate (4H-SiC \{10$\bar{1}$1\} at 2θ = 34.84°, ψ = 75.17°). The strong pole at the center originates both from r-B_xC\{10$\bar{1}$4\} and the tail of 4H-SiC\{0001\} (2θ = 35.6°, ψ = 0°).

the crystal structure of r-B_xC which is rhombohedral and (2) the polycrystalline nature of the textured films, which would usually exhibit a fiber texture without symmetry. The five-fold symmetry originates from the tendency of r-B_xC to form five-fold twinning (Fig. S3‡).[11,12,16] However, upon closer inspection of the five broad poles at $\psi \approx 60°$, reveals the further division into three distinct peaks within each of these five broad poles. This is consistent with the fact that five and six are non-divisible: for a given family of the directions of a five-fold crystal, can only be aligned with one of the ⟨11$\bar{2}$0⟩ directions of 4H-SiC. As such, an alignment along [11$\bar{2}$0], [1$\bar{2}$10] and [$\bar{2}$110], will result in three adjacent 5-fold patterns as can be seen in Fig. 8. Furthermore, due to the lack of axial symmetry of five-fold objects (*e.g.*, a pentagon) there are two ways two align a five-fold crystal along a given direction (*e.g.*, the apex of a pentagon pointing towards either 4H-SiC[11$\bar{2}$0] or 4H-SiC[$\bar{1}\bar{1}$20]), so that one pole pattern is centrosymmetric with respect to the other. In our case, this is observed in Fig. 8 where poles of much fainter intensity can be found between the more intense poles of the five-fold patterns. As a result, the ring pattern comprises 5 (r-B_xC twinning) × 3 (4H-SiC symmetry axes) × 2 (lack of axial symmetry of 5-fold objects) = 30 poles (Fig. S4‡). The fortuitous varying intensity of the pattern brings to light that these five-fold twinned crystals or domains grow along each 11$\bar{2}$0 axes of the 4H-SiC surface in a heteroepitaxial fashion. The third pattern at the center of the pole figure is the superpositions of the last of the three B_xC\{10$\bar{1}$4\} poles ($\psi \approx 7°$) but are shadowed by the strong 4H-SiC(0001) pole ($\psi \approx 0°$).

From top-view scanning electron microscopy (Fig. 9), the films deposited at 1100 °C appear to comprise nodular grains (Fig. 9a). The films deposited between 1200 and 1400 °C (Fig. 9b–d) show highly twinned grains with a more pronounced faceting with increasing temperature. The grain size is around 1 μm. The surface morphology of these films is consistent with the texture evolution of the film. The crystallites of the films deposited at 1200 °C (Fig. 9b) and 1300 °C (Fig. 9c) appear as square-based pyramids. This is associated with films with a strong [02$\bar{2}$1] texture. At 1400 °C (Fig. 9d), the films appear porous and some of the grains with 5-fold twinning are visible, as expected from the pole figure of the [10$\bar{1}$4] orientated films. At 1500 °C (Fig. 9e), the boron carbide grains do not show preferred orientation.

Finally for comparison, the elemental composition of the film on the *Si*-face at 1300 °C determined using ToF-ERDA also yielded a ratio of 4 : 1 (B – 79.4% ± 0.7%, C – 20.5% ± 0.3%) with around 0.1% of O incorporation and the absence of H as it is below the detection limit of the instrument.

Discussion

As observed, the orientation of the boron carbide films on silicon carbide depends on the surface termination, the temperature, and the residence time. The demonstration of epitaxial growth of r-B_4C on 4H-SiC(000$\bar{1}$) from 1300 °C supports this, while all films deposited on 4H-SiC(0001) were found to be polycrystalline at the studied temperatures.

Open Access Article. Published on 30 2022. Downloaded on 29.09.2024 10:23:06.
This article is licensed under a Creative Commons Attribution 3.0 Unported Licence.

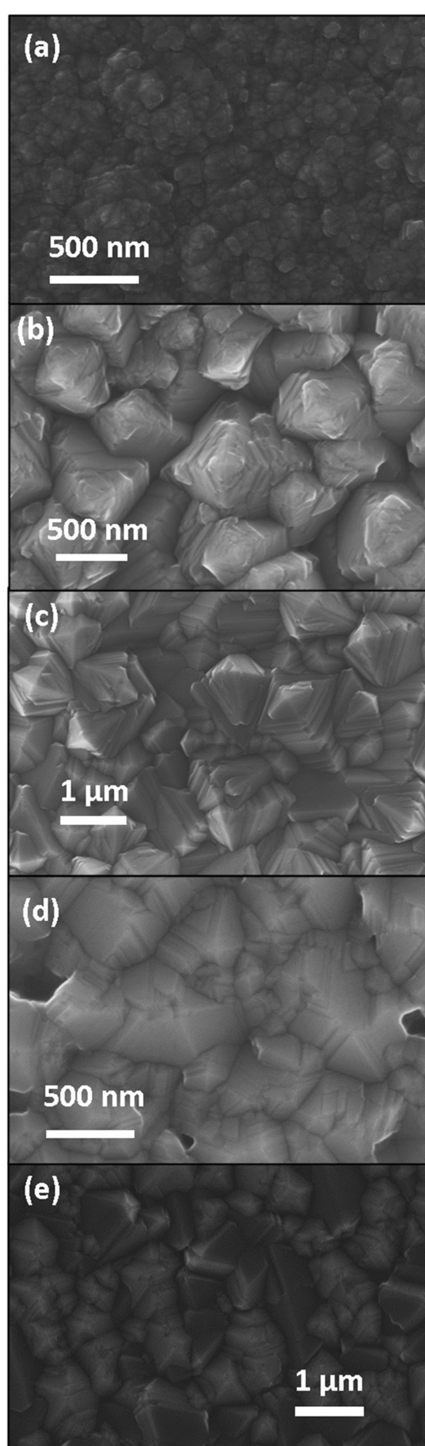

Fig. 9 Plan view SEM of rhombohedral boron carbide deposited at (a) 1100 °C, (b) 1200 °C, (c) 1300 °C, (d) 1400 °C and, (e) 1500 °C on 4H-SiC (0001).

In comparison to structurally similar materials such as rhombohedral boron subphosphide ($B_{12}P_2$) and subarsenide ($B_{12}As_2$), the threshold temperature for epitaxial growth for r-B_xC is comparable to the one reported for the CVD of $B_{12}P_2$ [17] and similar structural variants such as twinning was observed in $B_{12}As_2$ [18–20] and $B_{12}P_2$ [17] epitaxy, albeit on on-axis *Si*-face 4H-SiC(0001). A notable difference is observed in the evolution of crystalline quality with temperature as seen from rocking curves measurements: the crystalline quality of $B_{12}P_2$ and $B_{12}As_2$ was reported to degrade from 1350 °C (ref. 21) and 1450 °C,[19] respectively, while the crystalline quality of r-B_xC continues improving even up to 1500 °C. This could be attributed to the formation of volatile P or PH_x (respectively As or AsH_x) species from the deposited film, which is less prone to occur in the case of carbon, albeit at the cost of forming graphite. Finally, the presence of two components in our rocking curves measurements further suggests that the crystallites of the epitaxial r-B_4C films initially grow well aligned with the substrate at the early stages of the growth and deviate slightly later on, as in ref. 22.

However, in spite of the similarities with $B_{12}P_2$ and $B_{12}As_2$, which are typically grown epitaxially on the *Si*-terminated face, epitaxial growth of r-B_4C was not achieved on 4H-SiC (0001).[17,19,23,24]With the exception of their orientation on either SiC termination, the r-B_4C films show identical crystal structures, composition at the same growth temperature (1300 °C) and temperature thresholds for graphite formation (1400 °C), which indicates that the observed differences can only be attributed to nucleation and not to the steady-state growth. To understand these observations, we consider the differences that are already known between the two terminations of silicon carbide and are relevant to the early stage of the deposition process, such as surface energy, and graphene formation or surface stability in H_2.

From a thermodynamics perspective, the surface energy of the C-face of silicon carbides polytype is lower (7.5 J m^{-2}) than that of the *Si*-face (18 J m^{-2}).[25] To our knowledge, there are no computed data of the surface energy for all r-B_4C facets. Nevertheless, considering the surface energy for boron carbide for the $(10\bar{1}1)$ planes (3.21 J m^{-2}, (ref. 26) 3.27 J m^{-2} (ref. 27)) and the surface energy for α-boron facets (1.9 to 3.6 J m^{-2}),[28] having a similar structure as r-B_4C, differing only in the absence the triatomic chains, one can conclude that they are lower than the surface energy of the C-face of 4H-SiC. Assuming the interfacial energy to be small for (0001)-oriented B_4C crystals on SiC(0001) and SiC$(000\bar{1})$ due to the small lattice mismatch, one would expect that both surfaces would allow epitaxial growth; although it can be argued that the surface energy of SiC(0001) is so high that multiple orientations of B_4C could grow in-spite of a higher interfacial energy, hence leading to polycrystalline growth. The issue with these energetic considerations is that they might not be valid at our growth conditions.

A consequence of the high energy of the *Si*-face is that it is highly unstable in pure and carbon-enriched hydrogen ambient between 1400–1580 °C,[29–31] which is similar to our experimental conditions. Under these conditions, the *Si* face tends to be subjected to heavy step-bunching, forming irregular macro steps and micro steps of variable height, as well as etch pits.[29–31] In contrast, the C-face is reported to be etched smoothly at these conditions forming only micro steps with an average height of 2.5 nm,[30] equivalent to 2.5 times the *c*-axis of

This journal is © The Royal Society of Chemistry 2022

a 4H-SiC unit cell and about twice the *c*-axis of a r-B_4C unit cell (12.065–12.175 Å).[32] These aspects could explain the different results obtained between the two SiC faces, the etching of the *Si*-face results in a complex topography, facilitating polycrystalline growth, while the steps after etching the C-face are close to lattice-matched to both the *c*- and *a*-axes of the r-B_4C unit cell.

Besides thermodynamic and morphological aspects, the chemistry at the SiC surfaces is also relevant, especially the role of carbon. Our growth conditions (1100–1500 °C, 7000 Pa and hydrocarbon by-product to hydrogen ratio in the order of 135 to 406 ppm, assuming 1 to 3 mole of ethylene (C_2H_4) per mole of TEB[33]) seem to be adequate for the growth of graphene at the 4H-SiC(0001) surface.[34] Formation of graphene is known to be even easier on 4H-SiC(000$\bar{1}$) surface due to the absence of the partially sp^3-bonded interfacial layer (so-called buffer layer) between graphene and SiC.[35] However, only the *Si*-face affords oriented graphene layers (from 1350 °C at our CVD conditions),[34] while the graphene layers grown on the C-face are usually randomly rotated with respect to the substrate.[35,36] If a few layers of graphene would be the enabler for epitaxial growth of r-B_xC, one would expect epitaxial growth on the *Si*-face and not on the C-face, which is contrary to our observations, suggesting that graphene does not play a role in the process.

We instead consider the possibility that our deposition process operates in a window where the substrate, especially the C-face, may act as a carbon source but at a rate that prevents the formation of graphene. The second source of carbon in our process is evidently TEB, or rather, its main decomposition by-product, C_2H_4;[33] the decomposition of which is kinetically slower but can ultimately lead to the formation of acetylene and in turn of pyrolytic graphite, if the temperature is high enough and/or the residence time long enough.[37–39] From our results, we note that when the *Si*-terminated surface is used with a relatively short residence time, the texture of the films varied strongly with temperature, while for longer residence time the [0003] orientation prevails, until graphite forms. We suggest that this can be explained by the fact that a delicate balance of carbon concentration at the 4H-SiC(0001) surface may be needed to promote the growth of boron carbide along the *c*-axis. At lower temperatures (1200 °C and below), the *Si*-face is not an efficient carbon source on its own and the decomposition rate of the C_2H_4 byproducts is slow, leading to growth along the [0003] orientation only for the longest residence times. Around 1300 °C the carbon concentration is adequate to promote nucleation along the *c*-axis, although the films remain polycrystalline. Above 1300 °C, graphite forms and consumes the carbon provided by the C_2H_4 byproducts and again prevents the films from growing along the *c*-axis. In contrast, the C-face would be a more efficient C-source, making the growth less depending on the carbon coming from the gas phase and less sensitive to the formation of graphite. While the details of how carbon is involved in the nucleation mechanisms of boron carbide are yet to be understood, the carbon at the SiC surfaces might play a more significant role in r-B_xC epitaxy than the surface energy considerations and step formation mentioned above, as epitaxial $B_{12}As_2$[19,23,24] and $B_{12}P_2$[17] can be prepared on 4H-SiC (0001).

Conclusion

Our study shows that rhombohedral boron carbide with a composition B_4C (ToF-ERDA) can grow epitaxially on 4H-SiC(000$\bar{1}$) at 1300 °C by CVD using triethylboron as single source precursor in H_2. The epitaxial relationships were r-B_4C(0001)[10$\bar{1}$0]‖ 4H-SiC(0001)[10$\bar{1}$0] as seen from pole figure measurements. XRD and SEM revealed that higher deposition temperature results in co-deposition of graphite, and lower deposition temperature results in polycrystalline boron carbide. Deposition on 4H-SiC(0001) resulted in polycrystalline r-B_xC with preferred orientation and amount of co-deposited graphite varying with the deposition temperature and the gas residence time in the CVD reactor. We suggest that these results are explained by the ability of the SiC surface to supply carbon for the initial growth of r-B_xC. These results give further insight on the influence of growth conditions for this material system and enable the use of epitaxial boron carbide thin films for their intended applications in electronic and thermoelectric devices.

Conflicts of interest

There are no conflicts to declare.

Acknowledgements

This work was supported by the Swedish Foundation for Strategic Research (SSF), Contract No. IS14-0027, Carl Trygger's Foundation for Scientific Research, Contract No. CTS 14:189, and by the Swedish Research Council (VR) under contracts; No. 2018-05499 and 2017-04164. H. H. and H. P. further acknowledge financial support from the Swedish Government Strategic Research Area in Materials Science on Functional Materials at Linköping University (Faculty Grant SFO-Mat-LiU No. 2009-00971). Accelerator operation was supported by Swedish Research Council VR-RFI (Contract No. 2019-00191).

References

1 H. Werheit, A. Leithe-Jasper, T. Tanaka, H. W. Rotter and K. A. Schwetz, Some properties of single-crystal boron carbide, *J. Solid State Chem.*, 2004, **177**, 575–579.
2 F. Thévenot, Boron Carbide A Comprehensive Review, *J. Eur. Ceram. Soc.*, 1990, **6**, 205–225.
3 M. Carrard, D. Emin and L. Zuppiroli, Defect clustering and self-healing of electron-irradiated boron-rich solids, *Phys. Rev. B: Condens. Matter Mater. Phys.*, 1995, **51**, 11270.

Open Access Article. Published on 30 2022. Downloaded on 29.09.2024 10:23:06.
This article is licensed under a Creative Commons Attribution 3.0 Unported Licence.

Open Access Article. Published on 30 2022. Downloaded on 29.09.2024 10:23:06. This article is licensed under a Creative Commons Attribution 3.0 Unported Licence.

4 D. Emin, Unusual properties of icosahedral boron-rich solids, *J. Solid State Chem.*, 2006, **179**, 2791–2798.
5 H. Werheit, H. Binnenbruck and A. Hausen, Optical properties of boron carbide and comparison with β-rhombohedral boron, *Phys. Status Solidi B*, 1971, **47**, 153–158.
6 H. Werheit, M. Laux, U. Kuhlmann and R. Telle, Optical Interband Transitions of Boron Carbide, *Phys. Status Solidi B*, 1992, **172**, K81–K86.
7 H. Werheit, On excitons and other gap states in boron carbide, *J. Phys.: Condens. Matter*, 2006, **18**, 10655–10662.
8 G. A. Slack, T. F. McNelly and E. A. Taft, Melt growth and properties of B6P crystals, *J. Phys. Chem. Solids*, 1983, **44**, 1009–1013.
9 S. Bakalova, *et al.*, Energy band structure and optical response function of icosahedral $B_{12}As_2$: A spectroscopic ellipsometry and first-principles calculational study, *Phys. Rev. B: Condens. Matter Mater. Phys.*, 2010, **81**, 4–13.
10 M. Bouchacourt and F. Thevenot, The correlation between the thermoelectric properties and stoichiometry in the boron carbide phase B4C-B10.5C, *J. Mater. Sci.*, 1985, **20**, 1237–1247.
11 B. Wei, *et al.*, Massive icosahedral boron carbide crystals, *J. Phys. Chem. B*, 2002, **106**, 5807–5809.
12 M. Imam, *et al.*, Gas Phase Chemistry of Trimethylboron in Thermal Chemical Vapor Deposition, *J. Phys. Chem. C*, 2017, **121**, 26465–26471.
13 P. D. Kervalishvili, S. O. Shalamberidze and Y. A. Bikovsky, Oriented boron carbide films produced by laser spraying, *AIP Conf. Proc.*, 1991, **231**, 524–527.
14 Ö. Danielsson, U. Forsberg, A. Henry and E. Janzén, Enlarging the usable growth area in a hot-wall silicon carbide CVD reactor by using simulation, *Mater. Sci. Forum*, 2001, **353–356**, 99–102.
15 K. Arstila, *et al.*, Potku – New analysis software for heavy ion elastic recoil detection analysis, *Nucl. Instrum. Methods Phys. Res., Sect. B*, 2014, **331**, 34–41.
16 M. Karaman, *Chemical Vapour Deposition of Boron Carbide*, 2007.
17 C. D. Frye, C. K. Saw, B. Padavala, R. J. Nikoli and J. H. Edgar, Hydride CVD Hetero-epitaxy of B 12 P 2 on 4H-SiC, *J. Cryst. Growth*, 2017, **459**, 112–117.
18 J. R. Michael, T. L. Aselage, D. Emin and P. G. Kotula, Structural variants in attempted heteroepitaxial growth of $B_{12}As_2$ on 6H-SiC (0001), *J. Mater. Res.*, 2005, **20**, 3004–3010.
19 R. Nagarajan, *et al.*, Crystal growth of $B_{12}As_2$ on SiC substrate by CVD method, *J. Cryst. Growth*, 2005, **273**, 431–438.
20 H. Chen, *et al.*, Defect structures in $B_{12}As_2$epitaxial layers grown on (0001) 6H-SiC, *J. Appl. Phys.*, 2008, **103**, 123508.
21 C. D. Frye, *et al.*, Suppression of Rotational Twins in Epitaxial B12P2 on 4H-SiC, *Cryst. Growth Des.*, 2018, **18**, 669–676.
22 H. Miyake, C. H. Lin, K. Tokoro and K. Hiramatsu, Preparation of high-quality AlN on sapphire by high-temperature face-to-face annealing, *J. Cryst. Growth*, 2016, **456**, 155–159.
23 R. H. Wang, *et al.*, Chemical vapor deposition of $B_{12}As_2$ thin films on 6H-SiC, *J. Electron. Mater.*, 2000, **29**, 1304–1306.
24 W. M. Vetter, R. Nagarajan, J. H. Edgar and M. Dudley, Double-positioning twinning in icosahedral $B_{12}As_2$ thin films grown by chemical vapor deposition, *Mater. Lett.*, 2004, **58**, 1331–1335.
25 M. Syväjärvi, R. Yakimova and E. Janzén, Wetting properties and interfacial energies in liquid phase growth of α-SiC, *Mater. Sci. Forum*, 1998, **264–268**, 159–162.
26 T. D. Beaudet, J. R. Smith and J. W. Adams, Surface energy and relaxation in boron carbide (101-1) from first principles, *Solid State Commun.*, 2015, **219**, 43–47.
27 J. D. Clayton, *et al.*, Deformation and Failure Mechanics of Boron Carbide–Titanium Diboride Composites at Multiple Scales, *JOM*, 2019, **71**, 2567–2575.
28 W. Hayami and S. Otani, The role of surface energy in the growth of boron crystals, *J. Phys. Chem. C*, 2007, **111**, 688–692.
29 S. Soubatch, *et al.*, Structure and Morphology of 4H-SiC Wafer Surfaces after H_2-Etching, *Mater. Sci. Forum*, 2005, **483–485**, 761–764.
30 J. Hassan, J. P. Bergman, A. Henry and E. Janzén, *In situ* surface preparation of nominally on-axis 4H-SiC substrates, *J. Cryst. Growth*, 2008, **310**, 4430–4437.
31 C. L. Frewin, C. Coletti, C. Riedl, U. Starke and S. E. Saddow, A comprehensive study of hydrogen etching on the major SiC polytypes and crystal orientations, *Mater. Sci. Forum*, 2009, **615–617**, 589–592.
32 T. L. Aselage and R. G. Tissot, Lattice Constants of Boron Carbides, *J. Am. Ceram. Soc.*, 1992, **75**, 2207–2212.
33 M. Imam, *et al.*, Gas phase chemical vapor deposition chemistry of triethylboron probed by boron–carbon thin film deposition and quantum chemical calculations, *J. Mater. Chem. C*, 2015, **3**, 10898–10906.
34 A. Michon, *et al.*, Effects of pressure, temperature, and hydrogen during graphene growth on SiC(0001) using propane-hydrogen chemical vapor deposition, *J. Appl. Phys.*, 2013, **113**, 203501.
35 K. V. Emtsev, F. Speck, T. Seyller, L. Ley and J. D. Riley, Interaction, growth, and ordering of epitaxial graphene on SiC{0001} surfaces: A comparative photoelectron spectroscopy study, *Phys. Rev. B: Condens. Matter Mater. Phys.*, 2008, **77**, 1–10.
36 U. Starke and C. Riedl, Epitaxial graphene on SiC(0001) and : From surface reconstructions to carbon electronics, *J. Phys.: Condens. Matter*, 2009, **21**, 134016.
37 G. D. Towell and J. J. Martin, Kinetic data from nonisothermal experiments: Thermal decomposition of ethane, ethylene, and acetylene, *AIChE J.*, 1961, **7**, 693–698.
38 A. Holmen, O. Olsvik and O. A. Rokstad, Pyrolysis of natural gas: chemistry and process concepts, *Fuel Process. Technol.*, 1995, **42**, 249–267.
39 K. Norinaga, V. M. Janardhanan and O. Deutschmann, Modeling of Pyrolysis of Ethylene, Acetylene, and Propylene at 1073–1373 K with a Plug-Flow Reactor Model, *Int. J. Chem. Kinet.*, 2007, 199–208.

This journal is © The Royal Society of Chemistry 2022